

Coupling Ferroelectric to colloidal Nanocrystals as a Generic Strategy to Engineer the Carrier Density Landscape

Mariarosa Cavallo, Erwan Bossavit, Sylvia Matzen, Thomas Maroutian, Rodolphe Alchaar, Tung Huu Dang, Adrien Khalili, Corentin Dabard, Huichen Zhang, Yoann Prado, Claire Abadie, James K Utterback, Jean Francois Dayen, Mathieu G. Silly, Pavel Dudin, Jose Avila, Emmanuel Lhuillier,* and Debora Pierucci

The design of infrared nanocrystals-based (NCs) photodiodes faces a major challenge related to the identification of barriers with a well-suited band alignment or strategy to finely control the carrier density. Here, this study explores a general complementary approach where the carrier density control is achieved by coupling an NC layer to a ferroelectric material. The up-and-down change in ferroelectric polarization directly impacts the NC electronic structure, resulting in the formation of a lateral pn junction. This effect is uncovered directly using nano X-ray photoemission spectroscopy, which shows a relative energy shift of 115 meV of the NC photoemission signal over the two different up- and down-polarized ferroelectric regions, a shift as large as the open circuit value obtained in the diode stack. The performance of this pn junction reveals enhanced responsivity and reduced noise that lead to a factor 40 increase in the detectivity value.

generally grown at temperatures >500 °C. In addition, the lack of epitaxy eases the spectral tunability and the coupling to the read-out circuit. Though clear progress on the performances has been achieved with detectivity values reaching 10^{11} Jones at room temperature (10^{12} Jones at 200 K)^[1-3] in the short-wave infrared and 10^{11} Jones at 80 K^[4-7] in the mid-wave infrared, only a very limited number of structures have been explored. Most devices based on PbS NCs rely on ZnO/n-type PbS/p-type thiol-treated small PbS NCs/Au stack,^[8,9] while for HgTe, the junction relies on HgTe/Ag₂Te.^[4] Moving beyond these established structures requires deep knowledge of the band alignment as well as setting up strategies for carrier

density control.^[10,11] It becomes of utmost interest to establish alternative methods to form pn junctions. Alternatives to the pn stack have already been proposed, including a field-effect transistor (FET) operated under large drain bias,^[12] multi-gated FET^[13,14] or coupling of NCs to a bulk III-V semiconductor.^[15] Methods based on gating suffer from two limitations. First, gating requires application of a DC bias,^[16] which consumes energy. Second, the additional gate electrode can add noise to the device, potentially ruining the benefit of carrier density control. The latter is a key problem that is unfortunately often

Introduction

Narrow bandgap nanocrystals (NCs) now offer an interesting alternative to epitaxially grown semiconductors for the design of infrared (IR) sensors. By lifting the constraint of epitaxial matching, NCs offer cost-effective growth. They reduce the substrate toxicity while enabling a more energy-effective growth due to the reduced growth temperature of NCs (<150 °C for IR material) compared to semiconductor thin films

M. Cavallo, E. Bossavit, R. Alchaar, T. H. Dang, A. Khalili, C. Dabard, H. Zhang, Y. Prado, C. Abadie, J. K Utterback, E. Lhuillier, D. Pierucci
Sorbonne Université
CNRS
Institut des NanoSciences de Paris
INSP, Paris F-75005, France
E-mail: el@insp.upmc.fr

E. Bossavit, M. G. Silly, P. Dudin, J. Avila
Synchrotron SOLEIL
L'Orme des Merisiers
Départementale 128, Saint-Aubin 91190, France
S. Matzen, T. Maroutian
Centre de Nanosciences et de Nanotechnologies
CNRS
Université Paris-Saclay
10 boulevard Thomas Gobert, Palaiseau 91120, France
J. F. Dayen
Université de Strasbourg
IPCMS-CNRS UMR 7504
23 Rue du Loess, Strasbourg 67034, France
J. F. Dayen
Institut Universitaire de France
1 rue Descartes, Paris Cedex 05 75231, France

 The ORCID identification number(s) for the author(s) of this article can be found under <https://doi.org/10.1002/adfm.202300846>

© 2023 The Authors. Advanced Functional Materials published by Wiley-VCH GmbH. This is an open access article under the terms of the Creative Commons Attribution-NonCommercial License, which permits use, distribution and reproduction in any medium, provided the original work is properly cited and is not used for commercial purposes.

DOI: 10.1002/adfm.202300846

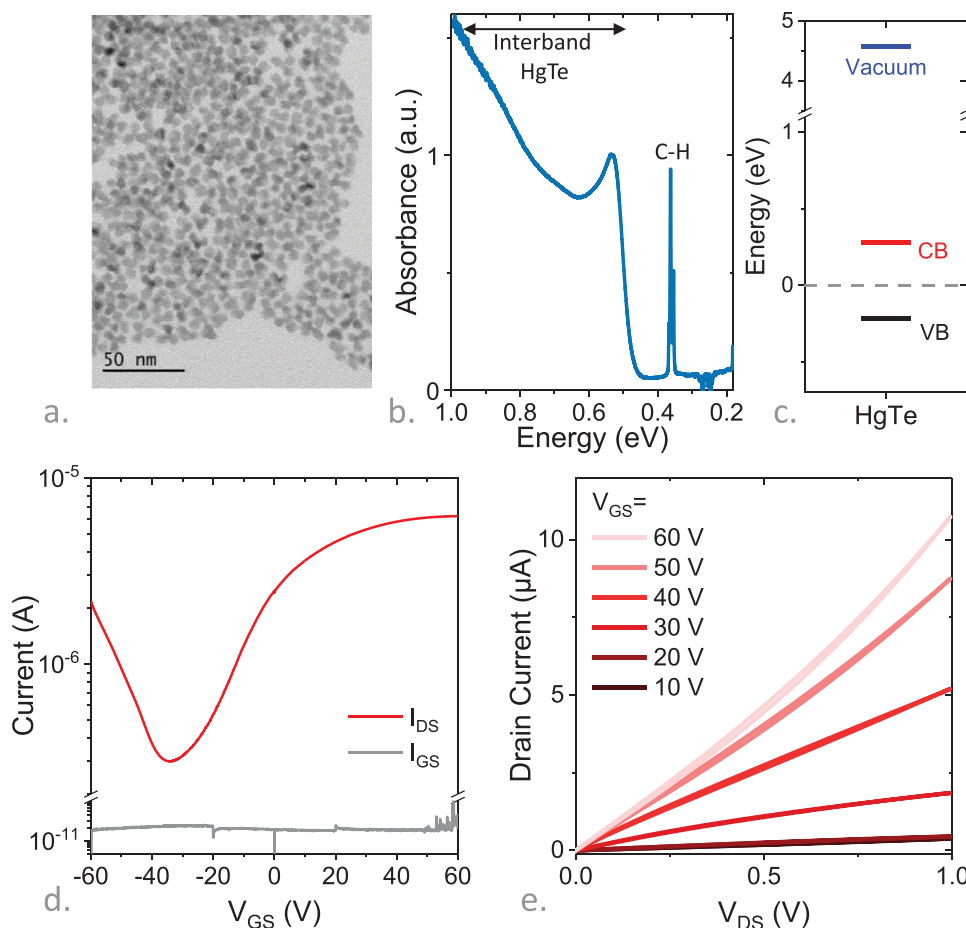


Figure 1. Optical and transport properties of HgTe infrared NCs. a). Transmission electron microscopy image of the HgTe NCs. b). Absorption spectrum of the HgTe NCs, measured at room temperature. c). Energy diagram (in red conduction band and in black valence band) with respect to the Fermi level used as energy reference. d). Transfer curve (i.e., drain and gate current as a function of applied gate bias under a 0.5 V drain-source bias). e). IV curve (i.e., drain current as a function of applied drain-source bias) under various positive gate biases. Transport measurements are conducted at 250 K.

swept under the rug. Thus, a field-induced strategy that does not require continuous application of bias would better be suited.

This can be obtained through the use of ferroelectric materials, where the inherent polarization of the material plays the role of the gate-induced electric field,^[17] as it has been proposed for 2D materials.^[18–20] However, there are very few reports in the literature dedicated to the coupling of NCs with ferroelectric materials.^[21] So far, ferroelectrics coupled to NCs have mostly been used as high-*k* material as their dielectric constant diverges as the temperature approaches the Curie temperature. Loi's group realized an FET with a gate made of a polymeric ferroelectric (i.e., a derivative of PVDF).^[22] Even higher dielectric constants can be obtained from perovskite oxides. In thin films of SrTiO₃ (STO), for example, the dielectric constant can be >10 000, enabling efficient gating with breakdown-free operation.^[23] However, in the case of STO, the Curie temperature being negative, the effect is only observed at cryogenic temperature (i.e., below 100 K). In both cases, the ferroelectric material has been used in its paraelectric phase, and there was no benefit from the remnant polarization. Here, we target the coupling of NCs with a ferroelectric layer whose polarization is further spatially designed to form a planar pn junction. While this

concept has been proposed for 2D materials,^[18,19,24–27] its implementation with NCs^[21] raised challenges since the solution processing of the active material may affect the written polarization. Here, we design a robust ferroelectric-NC heterostructure made of PbZr_{0.2}Ti_{0.8}O₃ (PZT) and HgTe NCs. The effect of the ferroelectric polarization on the band offsets of HgTe is revealed using nano-beam X-ray photoemission spectroscopy. Finally, we demonstrate the possibility of building a photodiode from this strategy and quantify how the ferroelectric substrate can enhance the IR detection properties of the material.

Results and Discussion

To design a planar pn junction, an ambipolar material is required, in which both electron and hole injection are possible. In addition, to be relevant for current developments in infrared optoelectronics, we choose to focus on HgTe NCs^[28] with a bandgap at $\approx 4000\text{ cm}^{-1}$ (or 0.5 eV or 2.5 μm , see **Figure 1b**). Such bandgap corresponds to extended short-wave infrared, a spectral range where InGaAs technology is no longer lattice matched on an InP substrate, making it more challenging to grow.

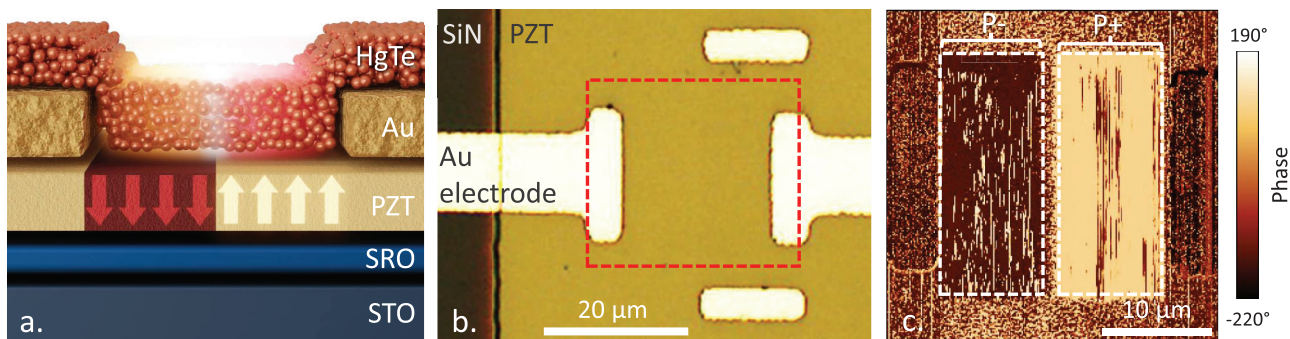


Figure 2. Hybrid ferroelectric-nanocrystal structure. a). Schematic of the STO/SRO/PZT/HgTe stack used as gate-less planar pn junction. b). Top-down optical microscopy view of the active area of the device. The red dashed lines correspond to the area of the PFM image presented in part c. c). PFM image (phase contrast) of the active area of the device highlights the presence of an up (P^+) and a down (P^-) polarized area within the PZT layer.

The particles are grown using the procedure developed by Keuleyan et al.,^[29] in which a mercury chloride precursor reacts with trioctylphosphine telluride in oleylamine used as a coordinating solvent. The particle size, in the 8–10 nm range (see transmission electron microscopy image in Figure 1a), is chosen to match the targeted bandgap and is mostly driven by the reaction temperature and duration. Using X-ray photoemission (Figures S4 and S5, Supporting Information), we have been able to determine the energy diagram of the material, see Figure 1c. The angle-integrated photoemission spectra allow to locate the energy of the valence band maximum with respect to the Fermi level of the semiconductor. The latter is close to the middle of the gap (Figure 1c), which supports the ambipolar character of the material for this given bandgap and surface chemistry. Here, we use HgCl_2 and mercaptoethanol to render the film conductive^[30,31] and prevent charging.

To further attest the ambipolar character of the material, we integrated it into a FET. For this purpose, interdigitated electrodes (see method section 1.3 in the supporting information) are patterned onto a Si/SiO₂ wafer with a top dielectric thickness of 300 nm. The transfer curve (Figure 1d) displays a rise of conductance under both hole (i.e., negative gate bias) and electron injection (i.e., positive gate bias, also see Figure 1e). The minimum of conductance appears at a negative gate bias, which suggests a residual n-type character in the absence of gate control.

Then, a ferroelectric thin film was prepared with precise control over the orientation of the ferroelectric polarization by piezoresponse force microscopy (PFM). Using pulsed laser deposition, a SrRuO₃ (SRO) layer was epitaxially grown on top of a SrTiO₃ (STO) substrate. The SRO behaves as a metallic layer and will be later used as an electrode to apply voltage and polarize the ferroelectric layer. The top layer is made of PZT,^[32] a ferroelectric with a Curie temperature well above room temperature. Though the PZT is a wide bandgap material, the low density of point defects makes the deposition of metallic electrodes over areas of $>1 \text{ mm}^2$ likely to generate an electrical short. This is why a Si₃N₄ dielectric layer was deposited on most of the PZT surface, except on the active areas, to prevent any electrical shorts between the large area of the contact pads and the SRO layer underneath. This dielectric layer surrounds the small active areas where the PZT surface is accessible. Finally, gold electrodes are deposited to enable transport in the NC layer. Before spin coating the NCs,

we use PFM to induce two ferroelectric domains in the PZT (see Figure 2c; Figure S3, Supporting Information) with opposite polarization. The domain is oriented up on the side of the electrode closer to two gold markers, see Figure 2b, whereas a downward domain is defined in the vicinity of another electrode. Then, the NC ink (i.e., a solution of NCs capped with short ligands enabling transport) concentration and deposition speed are tuned to form a $\approx 50 \text{ nm}$ thick film. The entire procedure is described in detail in Figure S2 (Supporting Information), and the layer structure of the fabricated device is schematized in Figure 2a.

To unveil the effect of ferroelectric polarization on the NC electronic structure, we use soft X-ray photoemission microscopy. A synchrotron beam is focused on the sample using a Fresnel Zone Plate (FZP), see a schematic of the experiment in Figure S6 (Supporting Information). The spot size on the sample surface is $\approx 700 \text{ nm}$, as characterized by 10–90% width of the knife-edge profile. The sample surface is imaged using raster scanning of sample position. For each point in raster, the photoelectrons are collected into an electron analyzer, giving access to their binding energies (BE) in absolute energy scale. The FZP operates at low photon energy (50–100 eV), where the beamline delivers the highest flux of photons. This is the reason why we choose to track a low binding energy core level: Hg 5d with a binding energy $\approx 8 \text{ eV}$, see Figure S4 (Supporting Information). On the same chip, a reference sample with no written domain (note that as-grown PZT is here polarized upward^[33]) and the test sample with up and down domains are both present, allowing imaging of both devices with the same NC film, see Figure 3a. In the reference part of the sample (Figure 3b), the BE value of the Hg5d state is homogeneous over the area defined by the two electrodes. However, in the case of the written device, the soft X-ray photoemission microscopy clearly reveals a contrast (Figure 3c) resulting from a shift of the Hg 5d binding energy, see Figure 3d,e.

The remnant polarization of the PZT film introduces an effective electric field at the interface, which can control the space charge distribution in the HgTe film. Over the area corresponding to a downward polarization (Figure 2c), the top surface of the ferroelectric is negatively charged, inducing an accumulation of positive charges at the interface with HgTe. As a consequence, an upward band bending will be present, which moves the valence band away from the Fermi level, making the material more

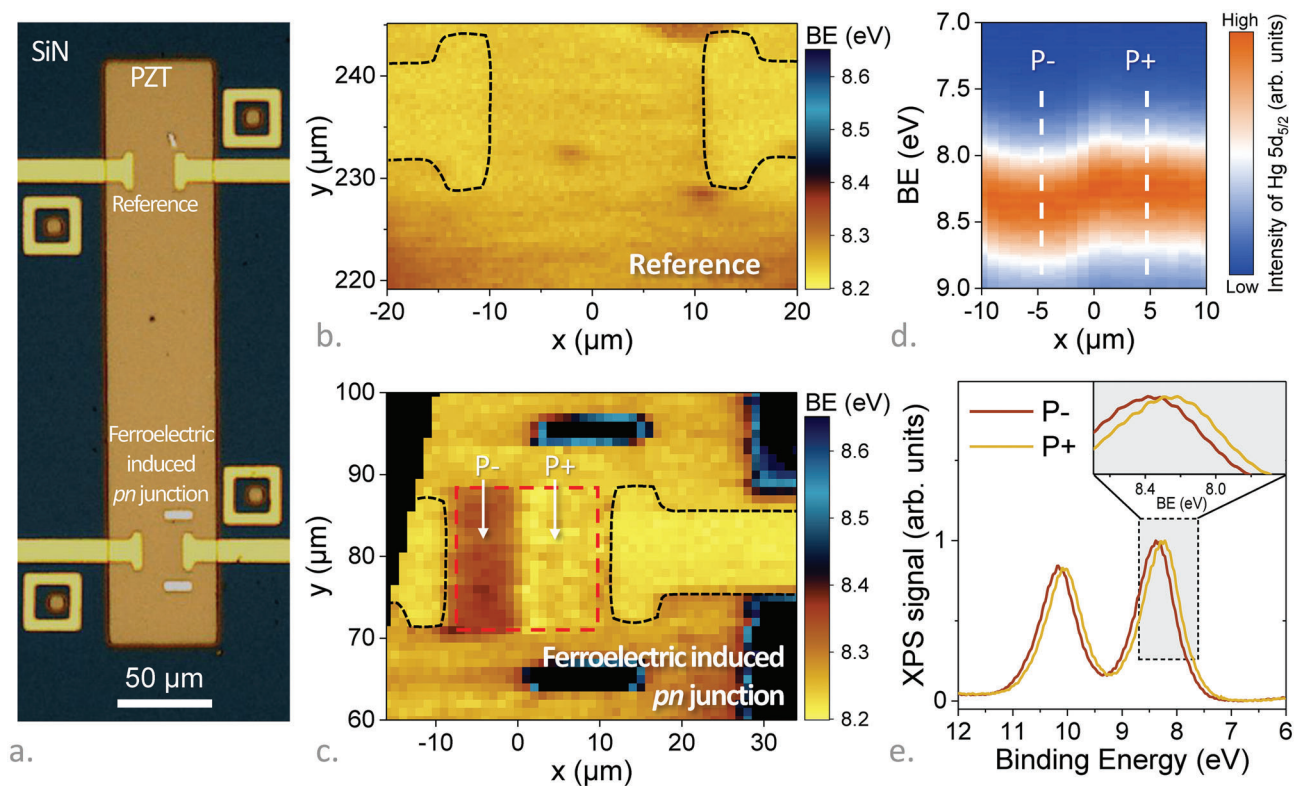


Figure 3. Effect of ferroelectric polarization on HgTe NCs electronic structure. a). Top-down view of the hybrid ferroelectric-HgTe NCs structure. The top device is used as reference (i.e., no domain is written on the PZT layer), while the bottom device is patterned as shown in Figure 2c. b). (resp. c.) Binding energy map of the Hg $5d_{5/2}$ state for the reference device (resp. for the patterned ferroelectric device), black dashed lines highlight the electrodes positions. d). Binding energy profile, after integration over y , of the Hg $5d_{5/2}$ state across the two electrodes for the device where the ferroelectric has been patterned. e). Corresponding integrated XPS spectra of the Hg 5d state in the areas of up and down polarization.

n-type. This effect is visible in the value of the BE of the Hg 5d state, which presents a shift of ≈ 115 meV toward the higher BEs (Figure 3c–e). An opposite situation is present in the area with an upward polarization (right side figure 3c–e), where the negative charges accumulation at the interface with the PZT induces a downward band bending (i.e., a lowering of BE) of the system making the holes the mobile charges.

Assuming a Fermi level in the middle of the gap, as revealed by XPS and transport measurements, the carrier density is given by $n_{\text{QD}} = 2 \cdot \exp(-E_G/2k_b T) = 6 \times 10^{-3} \ll 1$, with $T = 250$ K the temperature, k_b the Boltzmann constant, and E_G the bandgap value. Therefore, the low carrier density enables the formation of a large depletion layer over which a band bending at the interface with the ferroelectric is formed. As a result, P^+ polarization is associated with a p-type behavior (and reversely P^- with n-type), which contrasts with what is observed in 2D transition metal dichalcogenides.^[24,34] This suggests that the polarization of the PZT is mediated at the interface by some intermediate dipoles as it has been observed for graphene coupled to a ferroelectric layer.^[35,36] In the case of graphene, the water adsorbed at the ferroelectric surface reverses the polarization. In our case, although water contribution cannot be excluded, ions and ligands present in the ink may also be involved.

Also note that the relatively long distance band bending that affects the top surface of the NC film efficiently enables the use of

surface-sensitive X-ray photoemission microscopy which probes only the few nanometers at the surface of the material layer.

The 115 meV energy shift can be further compared to the open-circuit voltage generated in a vertical diode stack. For HgTe, the most typical diode stack relies on HgTe/Ag₂Te heterojunction,^[4] the open-circuit voltage depends on the bandgap value and is found to be ≈ 200 mV for HgTe with bandgap at 0.7 eV (Figure S1, Supporting Information) and drops to ≈ 50 mV for a 250 meV bandgap.^[1,2,7] In our case, the bandgap is intermediate ($E_G = 0.5$ eV), making the observed shift quite similar to the quasi-Fermi level splitting achieved in the best current diodes for this material.

Now that the coupling between the ferroelectric layer and the NC film has been demonstrated, we aim to test its potential for designing devices such as pn junctions. We first probe the transport for the reference device and the ferroelectric-induced junction. While the reference sample presents a symmetric IV curve (Figure 4a), the written device clearly shows a rectifying behavior, with a current asymmetry reaching above 50. Since both contacts are made of gold, we can confidently attribute the asymmetry to the designed P^+/P^- interface rather than to the metal semiconductor barrier. Note that the in-plane electric field used during the electrical measurement is of the order of 1 kV cm^{-1} , an electric field that is 600 times weaker than the field used to write the domain via the PFM tip, thus a full flip of the ferroelectric orientation is not expected during the measurement of the IV curve.

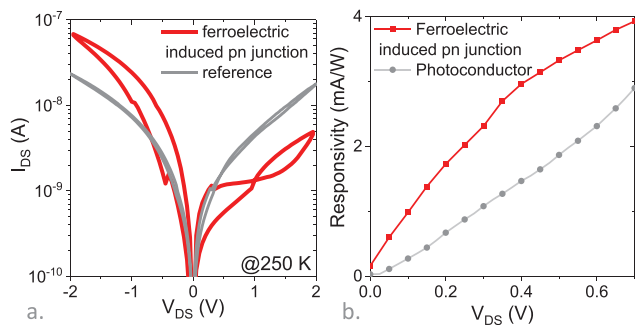


Figure 4. Optoelectronic properties of the ferroelectric induced pn junction. a). IV curve of the reference (both polarizations are P+ in this case) and ferroelectric induced pn junction. Note that discontinuities occurring at 1 nA are due to a change of range of the sourcemeter. b). Responsivities of the two devices as a function of drain-source bias (at 250 K). Illumination is obtained with a 1.55 μm laser diode.

However, the presence of hysteresis may be explained by a partial change of the orientation or alternatively by ions (coming from the ligand exchange procedure) migration.

The diode operates in the forward mode when a positive potential is connected to the upward polarization (i.e., most p-type material). The benefit of the pn junction can also be seen on the photoresponse curve, where higher responsivity is achieved with the pn junction as opposed to the symmetric photoconductor thanks to the built-in potential, see Figure 4b. The detectivity (i.e., the signal-to-noise ratio, $D^* = \frac{R\sqrt{A}}{i_n}$, with R the responsivity, A the optical area of the device and i_n the current noise spectral density) of the pn junction is greatly enhanced compared to the reference sample, being ≈ 40 times higher. Since the responsivity (Figure 4b) is at most improved by a factor of ≈ 2 , the increased detectivity is resulting from the reduced noise, see Figure S7 (Supporting Information). Again, the built-in potential allows to shift the device operation from a $1/f$ limited noise in the case of the photoconductive operation to a white noise limited device in the case of the pn junction. However, the absolute detectivity remains weak ($D^* \approx 2 \times 10^8$ Jones), mostly due to the low absorption and non-optimized geometry of the device (with long-distance transport poorly compatible with hopping conduction). Indeed, here, the device geometry has been optimized to be compatible with the soft X-ray photoemission microscopy analysis. Certainly, shrinking the size of the device closer to the diffusion length limit^[30,37] or the introduction of photonic resonator to focus light^[23,38–41] on a film thickness over which substrate effect is still impacting the doping will enhance the device's performance.

Conclusion

To summarize, we have demonstrated the coupling between a ferroelectric material and a nanocrystal film. Direct imaging of the coupling is obtained using nanobeam X-ray photoemission microscopy. We observe a 115 meV shift of the NC core level with polarization, which is entirely spatially correlated to the polarization domains. This correction corresponds to $1/4$ of the material bandgap and is as strong as the quasi-Fermi level shift observed in the best diodes based on this material. The potential of this strategy for the design of planar pn junctions is tested

and leads to a strongly rectifying behavior for the IV curve. Moreover, we observe an enhanced photoresponse and a reduced noise thanks to the built-in potential. This study opens up the field of hybrid structures where ferroelectric materials will be used as a gateless/consumption-less strategy for controlling carrier density. Future efforts will also have to deal with the limited production of sample resulting from the combination of PLD and PFM writing and methods compatible with larger substrate formats will have to be tested.

Acknowledgments

The project was supported by ERC grant blackQD (grant no 756225) and AQDtive (grant no 101086358). The author acknowledges the use of clean-room facilities from the "Centrale de Proximité Paris-Centre". Research at the Center for Nanoscience and Nanotechnology was supported by the French RENATECH network. This study was supported by French state funds managed by the ANR more specifically within the grants IPER-Nano2 (ANR-18-CE30-0023), Copin (ANR-19-CE24-0022), Frontal (ANR-19-CE09-0017), Graskop (ANR-19-CE09-0026), NITQuantum (ANR-20-ASTR-0008-01), Bright (ANR-21-CE24-0012-02), MixD-ferro (ANR-21-CE09-0029), Quicktera (ANR-22-CE09-0018) and Operatwist (ANR-22-CE09-003-7-01). This project had received financial support from the CNRS through the MITI interdisciplinary programs (project within).

Supporting Information

Supporting Information is available from the Wiley Online Library or from the author.

Conflict of Interest

The authors declare no conflict of interest.

Data Availability Statement

The data that support the findings of this study are available from the corresponding author upon reasonable request.

Keywords

ferroelectrics, infrared, nanocrystals, pn junctions

Received: January 22, 2023

Revised: April 21, 2023

Published online:

- [1] P. Rastogi, E. Izquierdo, C. Gréboval, M. Cavallo, A. Chu, T. H. Dang, A. Khaili, C. Abadie, R. Alchaar, S. Pierini, H. Cruguel, N. Witkowski, J. K. Utterback, T. Brule, X. Z. Xu, P. Hollander, A. Ouerghi, B. Gallas, M. G. Silly, E. Lhuillier, *J. Phys. Chem. C* **2022**, 126, 13720.
- [2] M. M. Ackerman, M. Chen, P. Guyot-Sionnest, *Appl. Phys. Lett.* **2020**, 116, 083502.

- [3] Y. Dong, M. Chen, W. K. Yiu, Q. Zhu, G. Zhou, S. V. Kershaw, N. Ke, C. P. Wong, A. L. Rogach, N. Zhao, *Adv. Sci.* **2020**, *7*, 2000068.
- [4] M. M. Ackerman, X. Tang, P. Guyot-Sionnest, *ACS Nano* **2018**, *12*, 7264.
- [5] X. Tang, M. M. Ackerman, M. Chen, P. Guyot-Sionnest, *Nat. Photonics* **2019**, *13*, 277.
- [6] S. Zhang, G. Mu, J. Cao, Y. Luo, Q. Hao, M. Chen, Y. Tan, P. Zhao, X. Tang, *Photonics Res* **2022**, *10*, 1987.
- [7] C. Gréboval, E. Izquierdo, C. Abadie, A. Khalili, M. Cavallo, A. Chu, T. H. Dang, H. Zhang, X. Lafosse, M. Rosticher, X. Z. Xu, A. Descamps-Mandine, A. Ouerghi, M. G. Silly, S. Ithurria, E. Lhuillier, *ACS Appl. Nano Mater* **2022**, *5*, 8602.
- [8] C.-H. M. Chuang, P. R. Brown, V. Bulović, M. G. Bawendi, *Nat. Mater.* **2014**, *13*, 796.
- [9] K. Lu, Y. Wang, Z. Liu, L. Han, G. Shi, H. Fang, J. Chen, X. Ye, S. Chen, F. Yang, *Adv. Mater.* **2018**, *30*, 1707572.
- [10] X. Xue, M. Chen, Y. Luo, T. Qin, X. Tang, Q. Hao, *Light Sci Appl* **2023**, *12*, 2.
- [11] S. C. Erwin, L. Zu, M. I. Haftel, A. L. Efros, T. A. Kennedy, D. J. Norris, *Nature* **2005**, *436*, 91.
- [12] U. N. Noubé, C. Gréboval, C. Livache, A. Chu, H. Majjad, L. E. Parra López, L. D. N. Mouafo, B. Doudin, S. Berciaud, J. Chaste, A. Ouerghi, E. Lhuillier, J.-F. Dayen, *ACS Nano* **2020**, *14*, 4567.
- [13] C. Gréboval, C. Dabard, N. Konstantinov, M. Cavallo, S.-S. Chee, A. Chu, T. H. Dang, A. Khalili, E. Izquierdo, Y. Prado, H. Majjad, X. Z. Xu, J.-F. Dayen, E. Lhuillier, *ACS Appl. Electron. Mater.* **2021**, *16*, 2335.
- [14] S.-S. Chee, C. Gréboval, D. V. Magalhaes, J. Ramade, A. Chu, J. Qu, P. Rastogi, A. Khalili, T. H. Dang, C. Dabard, Y. Prado, G. Patriarche, J. Chaste, M. Rosticher, S. Bals, C. Delerue, E. Lhuillier, *Nano Lett.* **2021**, *21*, 4145.
- [15] A. Khalili, C. Abadie, T. H. Dang, A. Chu, E. Izquierdo, C. Dabard, C. Gréboval, M. Cavallo, H. Zhang, S. Pierini, *Appl. Phys. Lett.* **2022**, *120*, 051101.
- [16] S. Gudjonsdottir, A. J. Houtepen, *Adv. Funct. Mater.* **2020**, *30*, 2004789.
- [17] J. J. Brondijk, K. Asadi, P. W. M. Blom, D. M. de Leeuw, *J. Polym. Sci., Part B: Polym. Phys.* **2012**, *50*, 47.
- [18] G. Wu, X. Wang, Y. Chen, S. Wu, B. Wu, Y. Jiang, H. Shen, T. Lin, Q. Liu, X. Wang, P. Zhou, S. Zhang, W. Hu, X. Meng, J. Chu, J. Wang, *Adv. Mater.* **2020**, *32*, 1907937.
- [19] J.-W. Chen, S.-T. Lo, S.-C. Ho, S.-S. Wong, T.-H.-Y. Vu, X.-Q. Zhang, Y.-D. Liu, Y.-Y. Chiou, Y.-X. Chen, J.-C. Yang, Y.-C. Chen, Y.-H. Chu, Y.-H. Lee, C.-J. Chung, T.-M. Chen, C.-H. Chen, C.-L. Wu, *Nat. Commun.* **2018**, *9*, 3143.
- [20] L. Lv, F. Zhuge, F. Xie, X. Xiong, Q. Zhang, N. Zhang, Y. Huang, T. Zhai, *Nat. Commun.* **2019**, *10*, 3331.
- [21] Y. H. Paik, H. S. Kojori, J.-H. Yun, S. J. Kim, *Mater. Lett.* **2016**, *185*, 247.
- [22] A. G. Shulga, L. Piveteau, S. Z. Bisri, M. V. Kovalenko, M. A. Loi, *Adv. Electron. Mater.* **2016**, *2*, 1500467.
- [23] C. Gréboval, A. Chu, D. V. Magalhaes, J. Ramade, J. Qu, P. Rastogi, A. Khalili, S.-S. Chee, H. Aubin, G. Vincent, S. Bals, C. Delerue, E. Lhuillier, *ACS Photonics* **2021**, *8*, 259.
- [24] R. Salazar, S. Varotto, C. Vergnaud, V. Garcia, S. Fusil, J. Chaste, T. Maroutian, A. Marty, F. Bonell, D. Pierucci, A. Ouerghi, F. Bertran, P. Le Fèvre, M. Jamet, M. Bibes, J. Rault, *Nano Lett.* **2022**, *22*, 9260.
- [25] S. Wu, Y. Chen, X. Wang, H. Jiao, Q. Zhao, X. Huang, X. Tai, Y. Zhou, H. Chen, X. Wang, S. Huang, H. Yan, T. Lin, H. Shen, W. Hu, X. Meng, J. Chu, J. Wang, *Nat. Commun.* **2022**, *13*, 3198.
- [26] S. Wu, G. Wu, X. Wang, Y. Chen, T. Lin, H. Shen, W. Hu, X. Meng, J. Wang, J. Chu, *J. Semicond* **2019**, *40*, 092002.
- [27] Z.-D. Luo, M.-M. Yang, Y. Liu, M. Alexe, *Adv. Mater.* **2021**, *33*, 2005620.
- [28] C. Gréboval, A. Chu, N. Goubet, C. Livache, S. Ithurria, E. Lhuillier, *Chem. Rev.* **2021**, *121*, 3627.
- [29] S. Keuleyan, E. Lhuillier, P. Guyot-Sionnest, *J. Am. Chem. Soc.* **2011**, *133*, 16422.
- [30] X. Lan, M. Chen, M. H. Hudson, V. Kamysbayev, Y. Wang, P. Guyot-Sionnest, D. V. Talapin, *Nat. Mater.* **2020**, *19*, 323.
- [31] B. Martinez, J. Ramade, C. Livache, N. Goubet, A. Chu, C. Gréboval, J. Qu, W. L. Watkins, L. Becerra, E. Dandeu, J. L. Fave, C. Méthivier, E. Lacaze, E. Lhuillier, *Adv. Opt. Mater.* **2019**, *7*, 1900348.
- [32] A. Zing, S. Matzen, K. Rani, T. Maroutian, G. Agnus, P. Lecoeur, *Appl. Phys. Lett.* **2022**, *121*, 232904.
- [33] E. Arenholz, G. van der Laan, A. Fraile-Rodríguez, P. Yu, Q. He, R. Ramesh, *Phys. Rev. B* **2010**, *82*, 140103.
- [34] X. Wang, P. Wang, J. Wang, W. Hu, X. Zhou, N. Guo, H. Huang, S. Sun, H. Shen, T. Lin, M. Tang, L. Liao, A. Jiang, J. Sun, X. Meng, X. Chen, W. Lu, J. Chu, *Adv. Mater.* **2015**, *27*, 6575.
- [35] X. Hong, J. Hoffman, A. Posadas, K. Zou, C. H. Ahn, J. Zhu, *Appl. Phys. Lett.* **2010**, *97*, 033114.
- [36] A. Lipatov, A. Fursina, T. H. Vo, P. Sharma, A. Gruverman, A. Sinitskii, *Adv. Electron. Mater.* **2017**, *3*, 1700020.
- [37] A. Chu, C. Gréboval, Y. Prado, H. Majjad, C. Delerue, J.-F. Dayen, G. Vincent, E. Lhuillier, *Nat. Commun.* **2021**, *12*, 1794.
- [38] T. H. Dang, C. Abadie, A. Khalili, C. Gréboval, H. Zhang, Y. Prado, X. Z. Xu, D. Gacemi, A. Descamps-Mandine, S. Ithurria, Y. Todorov, C. Sirtori, A. Vasanelli, E. Lhuillier, *Adv. Opt. Mater.* **2022**, *10*, 2200297.
- [39] C. Abadie, L. Paggi, A. Fabas, A. Khalili, T. H. Dang, C. Dabard, M. Cavallo, R. Alchaar, H. Zhang, Y. Prado, *Nano Lett.* **2022**, *22*, 8779.
- [40] Y. Luo, S. Zhang, X. Tang, M. Chen, *J. Mater. Chem. C* **2022**, *10*, 8218.
- [41] B. Zhu, M. Chen, Q. Zhu, G. Zhou, N. M. Abdelazim, W. Zhou, S. V. Kershaw, A. L. Rogach, N. Zhao, H. K. Tsang, *Adv. Mater. Technol.* **2019**, *4*, 1900354.